Calcite-Assisted Localization and Kinetics (CLocK) Microscopy

Joseph W. Monaghan[†§], Zachary J. O'Dell[†§], Sanjay Sridhar[†], Bianca Paranzino[†], Vignesh Sundaresan[‡*], Katherine A. Willets[†*]

†Department of Chemistry, Temple University, Philadelphia, Pennsylvania 19122, USA

‡Department of Chemistry and Biochemistry, University of Mississippi, University, Mississippi 38677, USA

Author Contributions

§ J.W.M. and Z.J.O. contributed equally to this work

*Corresponding Authors

Katherine A. Willets: kwillets@temple.edu

Beury Hall 1901 N 13th St, Philadelphia, PA 19122, USA

Vignesh Sundaresan: vsundare@olemiss.edu

Coulter Hall 140 University Avenue, University, MS 38677, USA

Abstract

Localization-based super-resolution imaging techniques have improved the spatial resolution of optical microscopy well below the diffraction limit, yet encoding additional information into super-resolved images, such as anisotropy and orientation, remains a challenge. Here we introduce calcite-assisted localization and kinetics (CLocK) microscopy, a multi-parameter super-resolution imaging technique easily integrated into any existing optical microscope setup at low cost and with straightforward analysis. By placing a rotating calcite crystal in the infinity space of an optical microscope, CLocK microscopy provides immediate polarization and orientation information while maintaining the ability to localize an emitter/scatterer with <10 nm resolution. Further, kinetic information an order of magnitude shorter than the integration time of the camera is encoded in the unique point spread function of a CLocK image, allowing for new mechanistic insight into dynamic processes such as single nanoparticle dissolution and single-molecule surface enhanced Raman scattering.

TOC Graphic

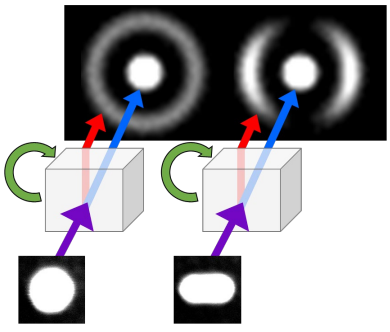

Localization-based super-resolution imaging is now well-established as a powerful tool to overcome the diffraction limit of light by analyzing single emitter point-spread functions (PSFs) to determine the spatial position associated with the point of highest intensity, leading to new insights in fields ranging from biology to material science. (1–13) The position of highest intensity is approximated as the location of the single emitter and, given sufficient signal to noise, can have spatial precision better than 10 nm. (14–17) Repeating the process for many single emitters allows for super-resolved images to be constructed, allowing us to break the resolution barrier of traditional optical microscopes and discover unseen structure and processes with nanoscale resolution.

One challenge with this approach is that a diffraction-limited spot encodes limited information about the emitter—typically only its spatial position and intensity (as in Figure S1A). However, additional information about the emitter, such as its orientation and extent of anisotropy, is desired for systems where rotational motion or dynamic changes in anisotropy can occur. (18–23) While it is possible to extract additional anisotropy and orientation information from a diffraction-limited image of a dipole emitter by fitting it to a 3-D dipole emission pattern, this requires extremely high signal-to-noise or image defocusing, which introduces complexities with localization analysis. (24–27) Alternative strategies for extracting orientation and polarization information involve using phase masks in the emission path of the microscope, but these are challenging to design, yield complex PSFs that can be non-intuitive to analyze, and are often sensitive to the emission wavelength of the species of interest as well as the optical properties of the microscope. (22,28) Inserting a rotating wedge polarizer into the emission path of a microscope simplifies this problem, but loses the simplicity of localizing a single emitter by fitting its

diffraction-limited emission. (29) A fourth approach involves splitting the diffraction-limited emission between two polarization channels, but this makes image registration difficult, especially in situations where the localized position of the emitter is polarization dependent (as our group has observed with fluorescent beads). (30–33) Moreover, splitting the emission is best suited for homogenous populations of dipole emitters (like single fluorophores) and is less successful in heterogeneous systems with variations in anisotropy (such as nanoparticles) where ambiguity in the polarization-resolved images can occur (Figure S1B).

In this work, we introduce calcite-assisted localization and kinetics (CLocK) microscopy, a multi-parameter super-resolution imaging technique that generates a polarization-averaged diffraction-limited image surrounded by a polarization-resolved ring, allowing both localization/intensity and anisotropy/orientation information to be extracted from a single image. CLocK microscopy relies on the birefringent nature of a rotating calcite crystal, which is inserted into the infinity space of the optical microscope (Figures 1A and S2). Light collected by the microscope objective passes through the calcite crystal and is split into two orthogonally-polarized rays: an ordinary ray ($o_{||}$) that continues along the original emission path and a spatially-displaced extraordinary ray ($e_{\perp}$), where || and $\perp$ represent the polarization states of the two rays relative to each other (Figure 1A). As the calcite crystal rotates at a rate equal to the acquisition rate of the imaging camera, the $e_{\perp}$ sweeps out a complete 360° ring around the stationary $o_{||}$, creating a unique PSF that resembles a ‘clock’, inspiring the name of the technique (for the sake of completeness, we note that this approach will work for other birefringent materials in addition to calcite).

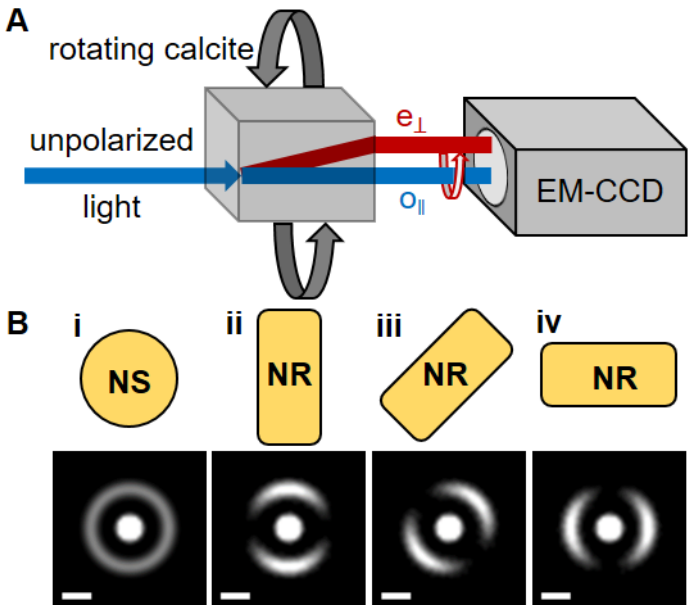

Figure 1. (A) Schematic representation of CLocK microscopy in which emission passes through a rotating calcite crystal, splitting it into mutually perpendicular polarizations: a stationary $o_{\parallel}$ ray and a spatially offset $e_{\perp}$ ray. As the calcite crystal rotates, the $e_{\perp}$ ray sweeps out a ring around the stationary $o_{\parallel}$ ray, producing a CLocK image. (B) Simulated CLocK images for an (i) isotropic nanosphere (NS) and (ii-iv) anisotropic nanorods (NRs) with varying orientations. The calcite crystal acts as polarization analyzer, leading to distinct patterns in the CLocK images. Scale bars 1 μm.

During the calcite crystal rotation, the linear polarizations probed by the $o_{\parallel}$ and the $e_{\perp}$ change as a function of calcite crystal orientation (θ), while remaining mutually perpendicular. For an isotropic object, such as a nanosphere (NS), the intensity of the $o_{\parallel}$ and $e_{\perp}$ will be equal at all values of θ, leading to uniform intensity in the $e_{\perp}$ ring that surrounds the polarization-averaged $o_{\parallel}$ image (Figure 1B-i). However, for anisotropic objects such as nanorods (NRs), which preferentially scatter light along their longitudinal axis, the intensity of $o_{\parallel}$ and $e_{\perp}$ will modulate as a function of θ, leading to an angle-dependent broken ring pattern in the $e_{\perp}$ that corresponds to the orientation (φ) of the longitudinal axis of the NR (Figure 1B-ii-iv). Optical images captured using CLocK microscopy reveal polarization and orientation information from the $e_{\perp}$ without sacrificing

the ability to localize the polarization-averaged centroid of the $o_{||}$ using traditional methods, such as fitting with a two-dimensional Gaussian (Figure S3). Moreover, the technique is compatible with multiple forms of optical microscopy, including dark field scattering, fluorescence, and Raman scattering (Figure S2 and *vide infra*).

To illustrate the power of the technique, Figure 2 compares traditional dark-field microscopy, dark-field CLocK microscopy, and scanning electron microscopy (SEM) for a mixture of Au NSs and NRs. While impossible to distinguish Au NSs from Au NRs in the dark-field microscopy image (Figure 2A), the unique PSFs produced in the CLocK image (Figure 2B) allow for the immediate differentiation of isotropic particles (Au NSs), which have a uniform $e_{\perp}$ pattern, and anisotropic particles (Au NRs), which have an angle-dependent $e_{\perp}$ pattern. Correlated SEM images confirm that the polarization and orientation information captured in the CLocK PSF reflects both the structure and orientation of the Au nanoparticles accurately (Figure 2C). Thus, from a single CLocK image, we can rapidly and non-destructively assess information about metal nanoparticle structure and orientation.

To quantify the degree of anisotropy and orientation of a particle, we use Equation 1:

$$I_{\theta} \propto 1 + Mcos\{2(\theta - \varphi)\} \quad (1)$$

where I_{θ} is the background-subtracted intensity of the $e_{\perp}$ as a function of θ, *M* is the modulation depth, and φ is the orientation of the particle (Figure S4). (34,35) An isotropic scatterer is expected to have a *M* value of 0, whereas a perfect dipole will have a *M* value of 1. Fitting particles 2 and 5 from Figure 2B to Equation 1 yields *M* values of 0.07 and 0.5, respectively, consistent with their SEM identification as a NS and a NR.

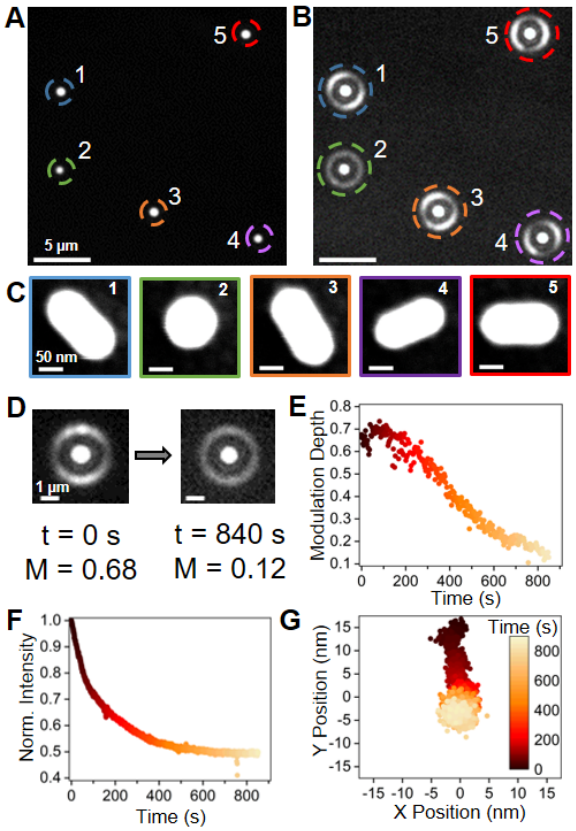

Figure 2. Comparison of (A) traditional dark-field, (B) dark-field CLocK, and (C) SEM images for a mixture of Au NSs and Au NRs. Optical images were acquired with an integration time of 300 ms. (D) Representative CLocK images of a Au NR before (t = 0 s) and after (t = 840 s) chemidissolution, showing that the Au NR transitions from an anisotropic rod-like structure to a more isotropic sphere-like structure after dissolution. (E-G) Changes in the (E) modulation depth, (F) scattering intensity, and (G) localized center-of-mass of the Au NR during chemidissolution. Scale bars: (A-B) 5 µm, (C) 50 nm, and (D) 1 µm.

Next, we demonstrate how CLocK allows us to track dynamic structural changes of nanoparticles in real time, by monitoring the chemidissolution of Au NRs in the presence of KI/I_2. Previous work has shown that NRs preferentially dissolve from their ends, resulting in the formation of spherical particles. (36,37) Figure 2D shows representative CLocK images of an Au NR (~120 nm long) before and after chemidissolution via KI/I_2 with a visual difference observed between the original anisotropic and the final isotropic CLocK images. Fitting the data to Equation 1, we

observe a smooth decrease in *M* from 0.68 to 0.12 (Figure 2E), supporting the previous literature observations that the Au NR becomes more spherical as the dissolution proceeds. The change in *M* is also accompanied by a drop in the integrated scattering intensity of the $o_{||}$ (Figure 2F), allowing us to monitor the kinetics of the chemidissolution process and indicating that the particle decreases in size during the dissolution process, consistent with previous reports. (23,38,39) Interestingly, by fitting the $o_{||}$ to a two-dimensional Gaussian and extracting the peak position, we observe a directional change in the center-of-mass over time (Figure 2G). If the NR was dissolving from each end at equal rates, we would expect the center-of-mass to remain unchanged during chemidissolution, even as the particle changed from rod-like to sphere-like (Figure S5A). However, not only do we observe the center-of-mass shift over time, but it also follows the orientation of the long axis of the Au NR, indicating that one end is etching faster than the other (Figure S5B). This mechanistic insight is hidden in traditional diffraction-limited images, yet is easily revealed through the multi-parameter analysis afforded by CLocK.

Further information can be obtained from CLocK by collecting color images. To illustrate this, CLocK images of Au nanoparticles were captured using a color camera (Figures 3A and S6). In Figure 3A, the $e_{\perp}$ pattern for a representative NS appears green at all θ due to the symmetry of the dipolar plasmon. Conversely, the $e_{\perp}$ pattern for two representative Au NRs show two different color contributions: red/orange light corresponding to the longitudinal plasmon mode and green light corresponding to the transverse plasmon mode. (29,40–43) For comparison, we note that the polarization-averaged diffraction-limited $o_{||}$ images of both NR-1 and NR-2 contain less visual spectral information, given that the scattered light is dominated by the red longitudinal plasmon

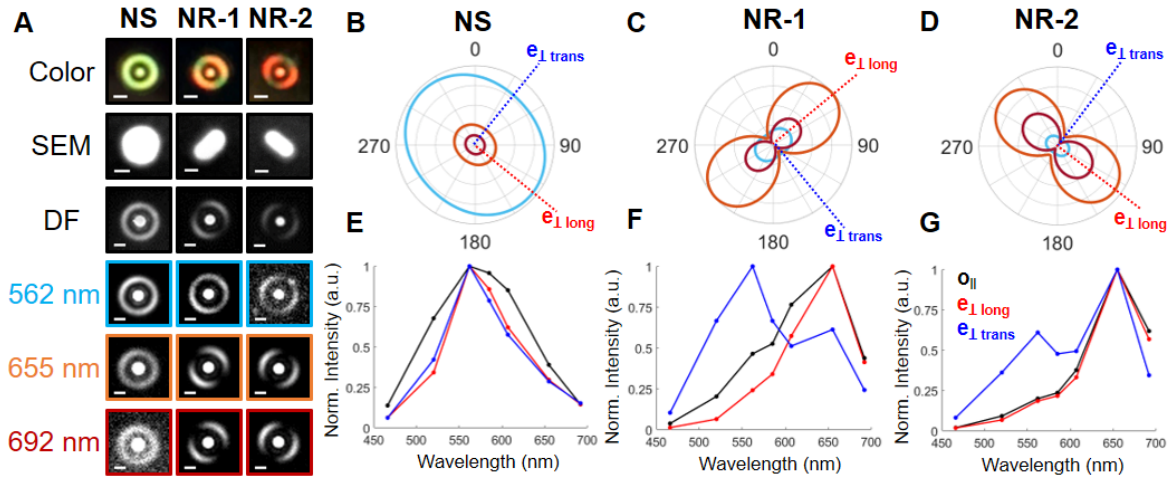

Figure 3. Comparison of spectral features found in CLocK images of a Au NS, large-width Au NR (NR-1), and small-width Au NR (NR-2). (A) From top to bottom: dark-field color CLocK images, SEM images, wavelength-averaged dark field (DF) CLocK images and spectrally-dependent dark field CLocK using bandpass filters centered at the wavelengths indicated. Images are shown at an optimal contrast to highlight the $e_{\perp}$ pattern. Scale bars: Color = 2 μm; SEM = 50 nm; DF = 1 μm. Optical images were acquired with an integration time of 300 ms. Bandpass filters: 562 ± 20 nm, 655 ± 20 nm, and 692 ± 20 nm. (B-D) Polar plots showing how the angle-dependent $e_{\perp}$ intensity changes as a function of bandpass filter wavelength. The data are normalized to the maximum scattering intensity and fit to Equation 1. Each trace in the polar plot is color coordinated to the bandpass filter labels in A. Each circle-tick of the polar plots is 0.25 normalized intensity units. (E-G) Normalized scattering intensity spectra of the intensity of $o_{\parallel}$ (black), $e_{\perp\ long}$ (red), and $e_{\perp\ trans}$ (blue) as a function of bandpass filter center wavelength. Data points are shown at the center wavelength of each filter and lines are drawn to guide the eye. Results from (B-D) and (E-G) agree well with polarization-resolved single-NP dark-field spectroscopy data (Figure S9).

mode of the nanoparticle. Thus, the color CLocK image captures structure-dependent spectral properties that are masked in a traditional-diffraction limited spot.

In addition to capturing color images, spectral information can be obtained by introducing wavelength-resolved imaging to CLocK microscopy. Bandpass filters were used to monitor the spectral evolution of the CLocK images from 466 to 692 nm (Figure 3A and S7). Next polar plots were constructed by fitting the normalized $e_{\perp}$ intensity vs. θ

to Equation 1 for images acquired at each wavelength, allowing us to visualize the spectrally-dependent evolution in anisotropy (Figures 3B-D, S7, S8). For example, analyzing the wavelength-dependent polar plots for a representative Au NS shows the scattered light is quasi-isotropic (*M* values below 0.2) over the entire wavelength range probed (Figures 3B and S8). In contrast, the polar plots for NR-1 and NR-2 show the scattered light becomes increasingly anisotropic with increasing wavelength, going from $M < 0.25$ to $M > 0.75$ (Figures 3, C-D, and S8).

Polarization-dependent spectra can also be extracted by means of spectrally-resolved imaging. Figure 3, E-G, shows the wavelength-dependent scattering intensity of the polarization-averaged $o_{||}$ (black data) as well as the intensity of the polarization-resolved light scattered along either the longitudinal axis ($e_{\perp\,long}$, red) or the transverse axis ($e_{\perp\,trans}$, blue), as determined from the polar plots in Figure 3, B-D. As expected, the Au NS spectra all have a single peak around 532 nm, indicating a single dipolar plasmon resonance (Figure 3E). On the other hand, the Au NRs show variations among the three spectra (Figure 3, F-G). The spectra along $e_{\perp\,long}$ (red data) are dominated by a single red peak, which corresponds to the longitudinal dipole mode, as expected. The spectra along $e_{\perp\,trans}$ (blue data) show two peaks: a peak in the blue-green region of the spectrum, which corresponds to the transverse plasmon mode, as well as a second red peak that aligns with the spectrum of the longitudinal mode. This agrees well with what has been previously shown in the literature, where the intensity of the transverse peak increases as a function of the NR diameter and the longitudinal peak intensity is suppressed along the transverse axis, but never completely disappears. (44) For comparison, Figure S9 shows polarization-resolved spectra taken using a grating spectrometer with a linear

polarizer placed in front of it, and the same trends are observed, indicating that using the calcite-crystal as a polarization analyzer does not introduce any artifacts in our spectra. We note that the polarization-averaged $o_{||}$ spectra (black data) are dominated by the red scattering from the longitudinal mode, hiding these polarization-dependent trends, further emphasizing the advantages of CLocK images over traditional diffraction-limited PSFs.

So far, we have only described the ability of CLocK to add polarization/anisotropy information to images (whether black and white or spectrally-filtered). However, CLocK images also encode temporal information below the integration time of the camera (τ) based on the $e_{\perp}$ arc length, addressing a growing interest in the field to capture short-lived events. (45,46) Figure 4A compares simulated CLocK images for isotropic emitters with varying on times (t_{on}) relative to the integration time of the camera (τ). For an event lasting the full integration time of the camera ($t_{on} = \tau$), the $e_{\perp}$ sweeps out a complete ring (Figure 4A-i). However, for events that are shorter than the integration time ($t_{on} < \tau$), the $e_{\perp}$ appears as an arc, where the length of the arc becomes shorter as the time of event decreases (Figure 4A, ii-iii). For sufficiently short on times (Figure 4A-iv), the arc becomes a diffraction-limited spot, which ultimately defines the temporal resolution of the technique.

To probe the temporal resolution in more detail, we trained a convolutional neural network (CNN) to extract the $e_{\perp}$ arc length from simulated CLocK images on (pseudo)isotropic emitters with M values between 0 – 0.2, where parameters such as absolute intensity, intensity-to-background ratio, $o_{\parallel}$ and $e_{\perp}$ Gaussian width, $o_{\parallel}$ center position, and $o_{\parallel}$ – $e_{\perp}$ distance, and orientation angle were allowed to randomly vary, while the parameter of interest (e.g. $e_{\perp}$ arc length) was systematically varied (see section 10 of

the SI for more details). The model uses polar coordinates to report temporal resolution, where an event with $t_{on} = \tau$ would be 360°, an event with $t_{on} = 0.25\tau$ would be 90°, etc. From these simulated data, we obtain a theoretical temporal resolution of 5.5°, corresponding to a minimum resolvable $t_{on} = \frac{\tau}{65}$.

To test this model on experimental data, we used a mechanical shutter to control the effective on-time of fluorescent events from single nanodiamonds. For fluorescent nanodiamonds with anisotropy values between $M = 0.0 – 0.2$ and signal-to-noise values ranging from 1.3 to 1.6, the trained CNN was able to extract $e_\perp$ arc lengths ranging from 5° - 360° with a root mean square error (RMSE) of 15°, or $t_{on} = \frac{\tau}{24}$ (corresponding to 6.7 ms temporal resolution with an integration time of 160 ms).

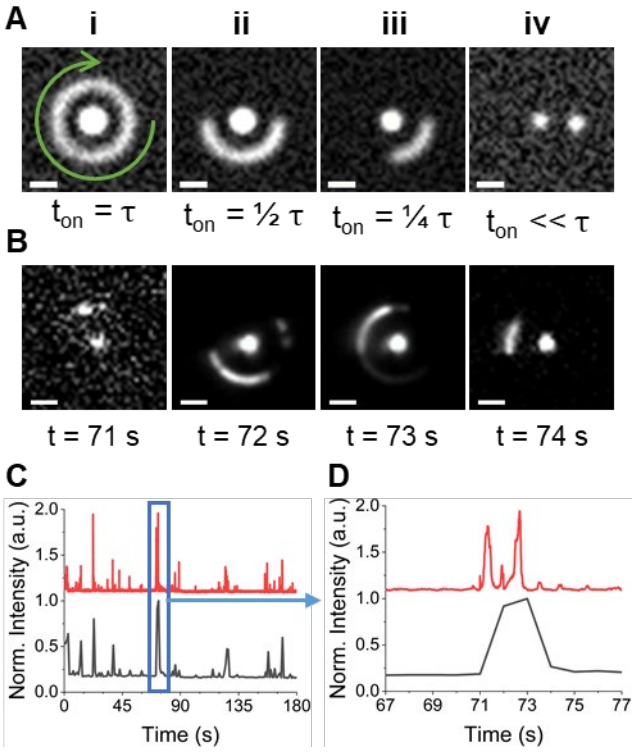

Figure 4. Kinetic information encoded in the $e_\perp$ arc length of CLocK images. (A) Simulated CLocK images showing kinetic events (t_{on}) lasting (i) τ, arc length = 360°, (ii) ½ τ, arc

length = 180°, (iii) ¼ τ, arc length = 90° and (iv) << τ, where τ is the time required to acquire an image and the arc length is expressed in polar coordinates. Scale bars = 1 μm. (B) Representative CLocK images for Rhodamine 6G SM-SERS events. Scale bars = 1 μm, optical images acquired with an integration time of 1 s. (C) Normalized intensity time-traces of the $o_{||}$ (black) and $e_{\perp}$ (red) for SM-SERS events on aggregated Ag colloid. (D) A subsection of the intensity time-traces from (C) is magnified to demonstrate the difference in temporal resolution provided by the $o_{||}$ and $e_{\perp}$. The portion of the time trace shown in (D) corresponds to the images shown in (B).

While the studies on fluorescent nanodiamonds allowed us to benchmark the temporal resolution of CLocK for isotropic emitters, we next explored single-molecule surface enhanced Raman scattering (SM-SERS) as a system where both fast temporal processes and polarized emission are present. (25,26,46–48) Moreover, unlike the previous data, where individual emitters/scatterers were well-spaced on the surface to avoid overlapping signals, the temporal fluctuations in SERS signals allows us to uniquely resolve the spatial origin of both the SERS signal and the underlying silver nanoparticle luminescence, which are both convolved in a single diffraction-limited spot. (14,15,49) Figure 4B shows several representative CLocK images of Rhodamine 6G (R6G) SM-SERS events on aggregated Ag colloid, where τ = 1s (additional events shown in Figure S11). In Figure 4C, normalized intensity time-traces using the $o_{||}$ (black) and the $e_{\perp}$ (red) are compared, revealing the added temporal resolution offered by analyzing the $e_{\perp}$. This temporal enhancement becomes even more apparent in the magnified sub-section of the time trace in Figure 4D: what appears as a single SM-SERS event lasting a few seconds in the $o_{||}$ data can be resolved as several separate and temporally distinct SM-SERS events using the $e_{\perp}$ data. However, due to the convolution of polarization and temporal information present in these short-lived SM-SERS events, we are currently unable to accurately quantify the temporal resolution observed. That said, based on our simulations above, we predict that our temporal resolution is no better than $\frac{\tau}{65}$ or 15 ms for the one

second integration times used in collecting these data. Although this temporal resolution can be experimentally improved by using shorter camera integration times, current limitations on the rotation speed of the motor do not allow us to access faster intensity fluctuations, as have been reported by others. (46)

One challenge that requires more exploration is how to extract polarization/orientation information from the short-lived events ($t_{on} < \tau$) revealed by CLocK (as in Figure 4B). To highlight this, Figures S11-S14 shows SM-SERS CLocK data on both a silver nanoparticle dimer and a larger multi-particle aggregate, as determined by CLocK. For the structure assigned as a dimer, we observe anisotropic dark field scattering ($M = 0.58$, $\varphi = 87°$), similar to the gold nanorods discussed above. Based on previous literature, we expect SM-SERS from a dimer to be polarized along the long axis, ([50]) and this behavior is observed for all SM-SERS events, even those shorter than τ (Figures S12-S13). Not only does the polarization of the SM-SERS further support our dimer assignment, but also highlights that for relatively simple structures, it is straightforward to interpret the polarization response.

On the other hand, our CLocK analysis suggests that the SM-SERS data shown in Figure 4B originates from a higher order nanoparticle aggregate (e.g. trimer or above). We make this assignment because (1) its dark field CLocK appears quasi-isotropic (unlike a dimer) and (2) the spatial origin of the aggregate luminescence is offset by >100 nm from the SERS hot spot (as we have previously observed in large aggregates, Figure S14).[15,51,52] From previous work, it is known that higher order aggregates can modify the output polarization of SM-SERS based on how the molecule couples to different plasmon modes within the aggregate. ([48,50,53]) Angle-dependent intensity analysis of images at t =

72 and 73 s from Figure 4B indicate that the two events appear to have different polarization responses, although neither have high quality fits to Equation 1 ($R^2 < 0.7$, Figure S14C, D). Interestingly, when we localized the SERS emission of these two frames by fitting the associated $o_{||}$ to a two-dimensional Gaussian, we found that the emission was spatially separated by 32 nm, which is larger than the expected precision of our SERS measurement (< 3 nm based on comparable signal; see Figure S3C and Table S1), suggesting that the molecule is exploring spatially distinct regions of the nanoparticle aggregate (Figure S14E). ([14,49,51,52]) We speculate that the R6G moved to a new location on the aggregate surface (as evidenced by the shift in its localized position), leading to a change in the polarization output of the SERS due to changes in how the molecular dipole couples to the plasmon modes of the aggregate. However, we note that in this regime, we cannot be completely quantitative about the polarization/orientation of the emission without having either events with $t_{on} > \tau$ and/or correlated nanoparticle structure information; this will be the subject of future work. Despite this challenge, these results highlight the wealth of information encoded in CLocK images that is unavailable in traditional diffraction-limited imaging and yet crucial for understanding these time-varying molecule-plasmon interactions.

In conclusion, we have introduced CLocK microscopy, a multi-parameter super-resolution imaging technique that allows the position, intensity, extent of anisotropy, and orientation of a single emitter/scatterer to be measured from a single image, while also offering fast temporal resolution for monitoring dynamic processes. We have demonstrated that CLocK allows for rapid structural discrimination in nanoparticle samples, and when combined with color or spectrally-resolved imaging, paints an even

clearer picture of differences in nanoparticle properties. Future work will focus on using color RGB images to extract spectral information and provide an even more complete particle-level analysis within a single dark field image. (18,41,54–60) To demonstrate the utility of CLocK, we showed two representative applications, nanorod chemidissolution and SM-SERS, where new mechanistic insight is revealed by the contemporaneous analyses of polarization and localization. Future work will focus on these two applications in more detail, as well as expanding our use of machine learning methods to train and analyze CLocK images. While we have successfully used machine learning to train CNNs to extract temporal information from CLocK images of isotropic emitters (Figure S10) and anisotropy/polarization information from CLocK images of non-blinking emitters (Figures S15 and S16), generating a sufficiently rigorous data set to train a CNN to extract these parameters from CLocK images with varying temporal and polarization characteristics (such as Figure 4B) remains an ongoing challenge. Despite this, we believe CLocK will prove useful across a wide range of applications, given that the technique is conceptually simple, relatively inexpensive to implement, works with existing super-localization codes, and is compatible with multiple forms of optical spectroscopy (including dark field, fluorescence, and Raman, as shown here), making it a universally useful imaging strategy for multi-parameter super-resolution imaging.

Experimental Methods

For all CLocK studies, a birefringent calcite crystal (Thor Labs, Mounted Calcite Beam Displacer, BD27 – 2.7 mm beam separation) housed in a motorized rotary mount (QIOPTIQ, Rotary Mount with Servo Motor) was placed in the infinity space of an inverted optical microscope (Olympus, IX-73, two-deck system) between the objective and tube lens. The rotation rate of the motorized rotary mount was controlled by a precision DC

voltage source (Stanford Research Systems, Model DC205) and monitored using an intelligent digital tachometer (Buyee, DT-2234C$^+$). Importantly, the rotation rate of the motorized rotary mount was set to equal the acquisition rate of the EM-CCD camera (Andor, iXon Life 897). Additional details about the microscope setups are discussed below, while descriptions of experimental procedures, including sample preparation, data collection, and data analysis can be found in the Supporting Information.

Acknowledgements

This work was supported by the U.S. National Science Foundation under grant number DMR-2003613. This research includes calculations carried out on HPC resources supported in part by the National Science Foundation through major research instrumentation grant number 1625061 and by the US Army Research Laboratory under contract number W911NF-16-2-0189. The authors would like to thank Natalia Y. Molina and Philip A. Reinhardt for their valuable discussions and suggestions throughout the experimental process.

Supporting Information Available: common abbreviations, reagents and materials used, CLocK microscopy theory, optical setups, additional experimental details and data analysis, discussion of CNNs used in CLocK microscopy

References

(1) Dean, K. M.; Palmer, A. E. Advances in Fluorescence Labeling Strategies for Dynamic Cellular Imaging. *Nat. Chem. Biol.* **2014**, *10* (7), 512–523. https://doi.org/10.1038/nchembio.1556.
(2) Sengupta, P.; van Engelenburg, S. B.; Lippincott-Schwartz, J. Superresolution Imaging of Biological Systems Using Photoactivated Localization Microscopy. *Chem. Rev.* **2014**, *114* (6), 3189–3202. https://doi.org/10.1021/cr400614m.
(3) Rust, M. J.; Bates, M.; Zhuang, X. Sub-Diffraction-Limit Imaging by Stochastic Optical Reconstruction Microscopy (STORM). *Nat. Methods* **2006**, *3* (10), 793–796. https://doi.org/10.1038/nmeth929.

(4) van de Linde, S.; Löschberger, A.; Klein, T.; Heidbreder, M.; Wolter, S.; Heilemann, M.; Sauer, M. Direct Stochastic Optical Reconstruction Microscopy with Standard Fluorescent Probes. *Nat. Protoc.* **2011**, *6* (7), 991–1009. https://doi.org/10.1038/nprot.2011.336.
(5) Biteen, J.; Willets, K. A. Introduction: Super-Resolution and Single-Molecule Imaging. *Chem. Rev.* **2017**, *117* (11), 7241–7243. https://doi.org/10.1021/acs.chemrev.7b00242.
(6) Betzig, E.; Patterson, G. H.; Sougrat, R.; Lindwasser, O. W.; Olenych, S.; Bonifacino, J. S.; Davidson, M. W.; Lippincott-Schwartz, J.; Hess, H. F. Imaging Intracellular Fluorescent Proteins at Nanometer Resolution. *Science* **2006**, *313* (5793), 1642–1645. https://doi.org/10.1126/science.1127344.
(7) Hauser, M.; Wojcik, M.; Kim, D.; Mahmoudi, M.; Li, W.; Xu, K. Correlative Super-Resolution Microscopy: New Dimensions and New Opportunities. *Chem. Rev.* **2017**, *117* (11), 7428–7456. https://doi.org/10.1021/acs.chemrev.6b00604.
(8) Lee, A.; Tsekouras, K.; Calderon, C.; Bustamante, C.; Pressé, S. Unraveling the Thousand Word Picture: An Introduction to Super-Resolution Data Analysis. *Chem. Rev.* **2017**, *117* (11), 7276–7330. https://doi.org/10.1021/acs.chemrev.6b00729.
(9) Shen, H.; Tauzin, L. J.; Baiyasi, R.; Wang, W.; Moringo, N.; Shuang, B.; Landes, C. F. Single Particle Tracking: From Theory to Biophysical Applications. *Chem. Rev.* **2017**, *117* (11), 7331–7376. https://doi.org/10.1021/acs.chemrev.6b00815.
(10) Möckl, L.; Moerner, W. E. Super-Resolution Microscopy with Single Molecules in Biology and Beyond–Essentials, Current Trends, and Future Challenges. *J. Am. Chem. Soc.* **2020**, *142* (42), 17828–17844. https://doi.org/10.1021/jacs.0c08178.
(11) Dhiman, S.; Andrian, T.; Gonzalez, B. S.; Tholen, M. M. E.; Wang, Y.; Albertazzi, L. Can Super-Resolution Microscopy Become a Standard Characterization Technique for Materials Chemistry? *Chem. Sci.* **2022**, *13* (8), 2152–2166. https://doi.org/10.1039/D1SC05506B.
(12) Willets, K. A. Super-Resolution Imaging of SERS Hot Spots. *Chem Soc Rev* **2014**, *43* (11), 3854–3864. https://doi.org/10.1039/C3CS60334B.
(13) Wöll, D.; Flors, C. Super-Resolution Fluorescence Imaging for Materials Science. *Small Methods* **2017**, *1* (10), 1700191. https://doi.org/10.1002/smtd.201700191.
(14) Stranahan, S. M.; Willets, K. A. Super-Resolution Optical Imaging of Single-Molecule SERS Hot Spots. *Nano Lett.* **2010**, *10* (9), 3777–3784. https://doi.org/10.1021/nl102559d.
(15) Weber, M. L.; Litz, J. P.; Masiello, D. J.; Willets, K. A. Super-Resolution Imaging Reveals a Difference between SERS and Luminescence Centroids. *ACS Nano* **2012**, *6* (2), 1839–1848. https://doi.org/10.1021/nn205080q.
(16) Weber, M. L.; Willets, K. A. Nanoscale Studies of Plasmonic Hot Spots Using Super-Resolution Optical Imaging. *MRS Bull.* **2012**, *37* (8), 745–751. https://doi.org/10.1557/mrs.2012.176.
(17) Willets, K. A. Super-Resolution Imaging of Interactions between Molecules and Plasmonic Nanostructures. *Phys. Chem. Chem. Phys.* **2013**, *15* (15), 5345–5354. https://doi.org/10.1039/C3CP43882A.
(18) Xiao, L.; Ha, J. W.; Wei, L.; Wang, G.; Fang, N. Determining the Full Three-Dimensional Orientation of Single Anisotropic Nanoparticles by Differential

Interference Contrast Microscopy. *Angew. Chem. Int. Ed.* **2012**, *51* (31), 7734–7738. https://doi.org/10.1002/anie.201202340.
(19) Peterman, E. J. G.; Sosa, H.; Goldstein, L. S. B.; Moerner, W. E. Polarized Fluorescence Microscopy of Individual and Many Kinesin Motors Bound to Axonemal Microtubules. *Biophys. J.* **2001**, *81* (5), 2851–2863. https://doi.org/10.1016/S0006-3495(01)75926-7.
(20) Gu, Y.; Won Ha, J.; E. Augspurger, A.; Chen, K.; Zhu, S.; Fang, N. Single Particle Orientation and Rotational Tracking (SPORT) in Biophysical Studies. *Nanoscale* **2013**, *5* (22), 10753–10764. https://doi.org/10.1039/C3NR02254D.
(21) Gu, Y.; Sun, W.; Wang, G.; Fang, N. Single Particle Orientation and Rotation Tracking Discloses Distinctive Rotational Dynamics of Drug Delivery Vectors on Live Cell Membranes. *J. Am. Chem. Soc.* **2011**, *133* (15), 5720–5723. https://doi.org/10.1021/ja200603x.
(22) Ding, T.; Lew, M. D. Single-Molecule Localization Microscopy of 3D Orientation and Anisotropic Wobble Using a Polarized Vortex Point Spread Function. *J. Phys. Chem. B* **2021**, *125* (46), 12718–12729. https://doi.org/10.1021/acs.jpcb.1c08073.
(23) Sundaresan, V.; Monaghan, J. W.; Willets, K. A. Visualizing the Effect of Partial Oxide Formation on Single Silver Nanoparticle Electrodissolution. *J. Phys. Chem. C* **2018**, *122* (5), 3138–3145. https://doi.org/10.1021/acs.jpcc.7b11824.
(24) Joshi, P. B.; Anthony, T. P.; Wilson, A. J.; Willets, K. A. Imaging Out-of-Plane Polarized Emission Patterns on Gap Mode SERS Substrates: From High Molecular Coverage to the Single Molecule Regime. *Faraday Discuss.* **2017**, *205*, 245–259. https://doi.org/10.1039/C7FD00163K.
(25) Stranahan, S. M.; Titus, E. J.; Willets, K. A. SERS Orientational Imaging of Silver Nanoparticle Dimers. *J. Phys. Chem. Lett.* **2011**, *2* (21), 2711–2715. https://doi.org/10.1021/jz201133p.
(26) Stranahan, S. M.; Titus, E. J.; Willets, K. A. Discriminating Nanoparticle Dimers from Higher Order Aggregates through Wavelength-Dependent SERS Orientational Imaging. *ACS Nano* **2012**, *6* (2), 1806–1813. https://doi.org/10.1021/nn204866c.
(27) Titus, E. J.; Willets, K. A. Accuracy of Superlocalization Imaging Using Gaussian and Dipole Emission Point-Spread Functions for Modeling Gold Nanorod Luminescence. *ACS Nano* **2013**, *7* (7), 6258–6267. https://doi.org/10.1021/nn4022845.
(28) Wu, T.; Lu, J.; Lew, M. D. Dipole-Spread-Function Engineering for Simultaneously Measuring the 3D Orientations and 3D Positions of Fluorescent Molecules. *Optica* **2022**, *9* (5), 505. https://doi.org/10.1364/OPTICA.451899.
(29) Schubert, O.; Becker, J.; Carbone, L.; Khalavka, Y.; Provalska, T.; Zins, I.; Sönnichsen, C. Mapping the Polarization Pattern of Plasmon Modes Reveals Nanoparticle Symmetry. *Nano Lett.* **2008**, *8* (8), 2345–2350. https://doi.org/10.1021/nl801179a.
(30) Lampe, A.; Haucke, V.; Sigrist, S. J.; Heilemann, M.; Schmoranzer, J. Multi-Colour Direct STORM with Red Emitting Carbocyanines. *Biol. Cell* **2012**, *104* (4), 229–237. https://doi.org/10.1111/boc.201100011.
(31) Bates, M.; Dempsey, G. T.; Chen, K. H.; Zhuang, X. Multicolor Super-Resolution Fluorescence Imaging via Multi-Parameter Fluorophore Detection. *ChemPhysChem* **2012**, *13* (1), 99–107. https://doi.org/10.1002/cphc.201100735.

(32) Jungmann, R.; Avendaño, M. S.; Woehrstein, J. B.; Dai, M.; Shih, W. M.; Yin, P. Multiplexed 3D Cellular Super-Resolution Imaging with DNA-PAINT and Exchange-PAINT. *Nat. Methods* **2014**, *11* (3), 313–318. https://doi.org/10.1038/nmeth.2835.
(33) Böning, D.; Wieser, F.-F.; Sandoghdar, V. Polarization-Encoded Colocalization Microscopy at Cryogenic Temperatures. *ACS Photonics* **2021**, *8* (1), 194–201. https://doi.org/10.1021/acsphotonics.0c01201.
(34) Adachi, T.; Brazard, J.; Ono, R. J.; Hanson, B.; Traub, M. C.; Wu, Z.-Q.; Li, Z.; Bolinger, J. C.; Ganesan, V.; Bielawski, C. W.; Vanden Bout, D. A.; Barbara, P. F. Regioregularity and Single Polythiophene Chain Conformation. *J. Phys. Chem. Lett.* **2011**, *2* (12), 1400–1404. https://doi.org/10.1021/jz200546x.
(35) Chang, W.-S.; Ha, J. W.; Slaughter, L. S.; Link, S. Plasmonic Nanorod Absorbers as Orientation Sensors. *Proc. Natl. Acad. Sci.* **2010**, *107* (7), 2781–2786. https://doi.org/10.1073/pnas.0910127107.
(36) Sun, S.; Gao, M.; Lei, G.; Zou, H.; Ma, J.; Huang, C. Visually Monitoring the Etching Process of Gold Nanoparticles by KI/I2 at Single-Nanoparticle Level Using Scattered-Light Dark-Field Microscopic Imaging. *Nano Res.* **2016**, *9* (4), 1125–1134. https://doi.org/10.1007/s12274-016-1007-z.
(37) Cheng, J.; Liu, Y.; Cheng, X.; He, Y.; Yeung, E. S. Real Time Observation of Chemical Reactions of Individual Metal Nanoparticles with High-Throughput Single Molecule Spectral Microscopy. *Anal. Chem.* **2010**, *82* (20), 8744–8749. https://doi.org/10.1021/ac101933y.
(38) Molina, N. Y.; Pungsrisai, T.; O'Dell, Z. J.; Paranzino, B.; Willets, K. A. The Hidden Role of the Supporting Electrode for Creating Heterogeneity in Single Entity Electrochemistry. *ChemElectroChem* **2022**, *9* (9). https://doi.org/10.1002/celc.202200245.
(39) Sundaresan, V.; Monaghan, J. W.; Willets, K. A. Monitoring Simultaneous Electrochemical Reactions with Single Particle Imaging. *ChemElectroChem* **2018**, *5* (20), 3052–3058. https://doi.org/10.1002/celc.201800715.
(40) Jain, P. K.; Lee, K. S.; El-Sayed, I. H.; El-Sayed, M. A. Calculated Absorption and Scattering Properties of Gold Nanoparticles of Different Size, Shape, and Composition: Applications in Biological Imaging and Biomedicine. *J. Phys. Chem. B* **2006**, *110* (14), 7238–7248. https://doi.org/10.1021/jp057170o.
(41) Huang, X.; El-Sayed, M. A. Gold Nanoparticles: Optical Properties and Implementations in Cancer Diagnosis and Photothermal Therapy. *J. Adv. Res.* **2010**, *1* (1), 13–28. https://doi.org/10.1016/j.jare.2010.02.002.
(42) Lohse, S. E.; Murphy, C. J. The Quest for Shape Control: A History of Gold Nanorod Synthesis. *Chem. Mater.* **2013**, *25* (8), 1250–1261. https://doi.org/10.1021/cm303708p.
(43) Halas, N. J.; Lal, S.; Chang, W.-S.; Link, S.; Nordlander, P. Plasmons in Strongly Coupled Metallic Nanostructures. *Chem. Rev.* **2011**, *111* (6), 3913–3961. https://doi.org/10.1021/cr200061k.
(44) Huang, Y.; Kim, D.-H. Dark-Field Microscopy Studies of Polarization-Dependent Plasmonic Resonance of Single Gold Nanorods: Rainbow Nanoparticles. *Nanoscale* **2011**, *3* (8), 3228. https://doi.org/10.1039/c1nr10336a.

(45) Wang, W.; Shen, H.; Shuang, B.; Hoener, B. S.; Tauzin, L. J.; Moringo, N. A.; Kelly, K. F.; Landes, C. F. Super Temporal-Resolved Microscopy (STReM). *J. Phys. Chem. Lett.* **2016**, *7* (22), 4524–4529. https://doi.org/10.1021/acs.jpclett.6b02098.
(46) Lindquist, N. C.; de Albuquerque, C. D. L.; Sobral-Filho, R. G.; Paci, I.; Brolo, A. G. High-Speed Imaging of Surface-Enhanced Raman Scattering Fluctuations from Individual Nanoparticles. *Nat. Nanotechnol.* **2019**, *14* (10), 981–987. https://doi.org/10.1038/s41565-019-0535-6.
(47) Shegai, T.; Brian, B.; Miljković, V. D.; Käll, M. Angular Distribution of Surface-Enhanced Raman Scattering from Individual Au Nanoparticle Aggregates. *ACS Nano* **2011**, *5* (3), 2036–2041. https://doi.org/10.1021/nn1031406.
(48) Shegai, T.; Li, Z.; Dadosh, T.; Zhang, Z.; Xu, H.; Haran, G. Managing Light Polarization via Plasmon–Molecule Interactions within an Asymmetric Metal Nanoparticle Trimer. *Proc. Natl. Acad. Sci.* **2008**, *105* (43), 16448–16453. https://doi.org/10.1073/pnas.0808365105.
(49) Weber, M. L.; Willets, K. A. Correlated Super-Resolution Optical and Structural Studies of Surface-Enhanced Raman Scattering Hot Spots in Silver Colloid Aggregates. *J. Phys. Chem. Lett.* **2011**, *2* (14), 1766–1770. https://doi.org/10.1021/jz200784e.
(50) Li, Z.; Shegai, T.; Haran, G.; Xu, H. Multiple-Particle Nanoantennas for Enormous Enhancement and Polarization Control of Light Emission. *ACS Nano* **2009**, *3* (3), 637–642. https://doi.org/10.1021/nn800906c.
(51) Titus, E. J.; Weber, M. L.; Stranahan, S. M.; Willets, K. A. Super-Resolution SERS Imaging beyond the Single-Molecule Limit: An Isotope-Edited Approach. *Nano Lett.* **2012**, *12* (10), 5103–5110. https://doi.org/10.1021/nl3017779.
(52) Weber, M. L.; Wilson, A. J.; Willets, K. A. Characterizing the Spatial Dependence of Redox Chemistry on Plasmonic Nanoparticle Electrodes Using Correlated Super-Resolution Surface-Enhanced Raman Scattering Imaging and Electron Microscopy. *J. Phys. Chem. C* **2015**, *119* (32), 18591–18601. https://doi.org/10.1021/acs.jpcc.5b05715.
(53) Chuntonov, L.; Haran, G. Maximal Raman Optical Activity in Hybrid Single Molecule-Plasmonic Nanostructures with Multiple Dipolar Resonances. *Nano Lett.* **2013**, *13* (3), 1285–1290. https://doi.org/10.1021/nl400046z.
(54) Biswas, S.; Nepal, D.; Park, K.; Vaia, R. A. Orientation Sensing with Color Using Plasmonic Gold Nanorods and Assemblies. *J. Phys. Chem. Lett.* **2012**, *3* (18), 2568–2574. https://doi.org/10.1021/jz3009908.
(55) Hao, J.; Xiong, B.; Cheng, X.; He, Y.; Yeung, E. S. High-Throughput Sulfide Sensing with Colorimetric Analysis of Single Au–Ag Core–Shell Nanoparticles. *Anal. Chem.* **2014**, *86* (10), 4663–4667. https://doi.org/10.1021/ac500376e.
(56) Huang, Y.; Ferhan, A. R.; Kim, D.-H. Tunable Scattered Colors over a Wide Spectrum from a Single Nanoparticle. *Nanoscale* **2013**, *5* (17), 7772. https://doi.org/10.1039/c3nr02718j.
(57) Jing, C.; Gu, Z.; Ying, Y.-L.; Li, D.-W.; Zhang, L.; Long, Y.-T. Chrominance to Dimension: A Real-Time Method for Measuring the Size of Single Gold Nanoparticles. *Anal. Chem.* **2012**, *84* (10), 4284–4291. https://doi.org/10.1021/ac203118g.

(58) Pan, Z. Y.; Zhou, J.; Zou, H. Y.; Li, Y. F.; Gao, P. F.; Huang, C. Z. In Situ Investigating the Size-Dependent Scattering Signatures and Sensing Sensitivity of Single Silver Nanocube through a Multi-Model Approach. *J. Colloid Interface Sci.* **2021**, *584*, 253–262. https://doi.org/10.1016/j.jcis.2020.09.121.
(59) Sweeney, C. M.; Nehl, C. L.; Hasan, W.; Liang, T.; Eckermann, A. L.; Meade, T. J.; Odom, T. W. Three-Channel Spectrometer for Wide-Field Imaging of Anisotropic Plasmonic Nanoparticles. *J. Phys. Chem. C* **2011**, *115* (32), 15933–15937. https://doi.org/10.1021/jp206157v.
(60) Zou, B.; Liu, Y.; Yan, X.; Huang, C. Gold Nanoparticles Based Digital Color Analysis for Quinidine Detection. *Chin. Sci. Bull.* **2013**, *58* (17), 2027–2031. https://doi.org/10.1007/s11434-013-5708-3.